Optical study of p-doping in GaAs nanowires for low-threshold and high-yield lasing

Juan Arturo Alanis,[†] Mykhaylo Lysevych,[‡,¶] Tim Burgess,[¶] Dhruv Saxena,[§,¶] Sudha Mokkapati,[‖,¶] Stefan Skalsky,[†] Xiaoyan Tang,[†] Peter Mitchell,[†] Alex S Walton,[⊥] Hark Hoe Tan,[¶] Chennupati Jagadish,[¶] and Patrick Parkinson[*,†]

†*School of Physics and Astronomy and the Photon Science Institute, The University of Manchester, Manchester, UK*

‡*Australian National Fabrication Facility, The Australian National University, Canberra, Australia*

¶*Department of Electronic Materials Engineering, Research School of Physics and Engineering, The Australian National University, Canberra, Australia*

§*The Blackett Laboratory, Department of Physics, Imperial College London, London, UK*

‖*School of Physics and Astronomy and the Institute for Compound Semiconductors, Cardiff University, Cardiff, UK*

⊥*School of Chemistry and the Photon Science Institute, The University of Manchester, Manchester, UK*

E-mail: patrick.parkinson@manchester.ac.uk

Abstract

Semiconductor nanowires suffer from significant non-radiative surface recombination, however, heavy p-type doping has proven to be a viable option to increase the radiative recombination rate and hence quantum efficiency of emission, allowing demonstration of room-temperature lasing. Using a large-scale optical technique, we have studied Zn-doped GaAs nanowires to understand and quantify the effect of doping on growth and lasing properties. We measure the non-radiative recombination rate (k_{nr}) to be $(0.14 \pm 0.04)\,\mathrm{ps}^{-1}$ by modelling the internal quantum efficiency (IQE) as a function of doping level. By applying a correlative method, we identify doping and nanowire length as key controllable parameters determining lasing behavior, with reliable room-temperature lasing occurring for $p \gtrsim 3 \times 10^{18}\,\mathrm{cm}^{-3}$ and lengths $\gtrsim 4\,\mu$m. We report a best-in-class core-only near-infrared nanowire lasing threshold of $\sim 10\,\mu\mathrm{J}$ cm^{-2} , and using a data-led filtering step, we present a method to simply identify sub-sets of nanowires with over 90% lasing yield.

Keywords

III-V Nanowire lasers, PL, Doping

Semiconductor nanowires have been widely studied for applications in optoelectronic integrated circuitry,[1–3] as photodetectors,[4] modulators[5,6] and coherent light sources;[7] they are excellent candidates for the fabrication of compact functional devices for operation at optical wavelength-scale offering the advantage of strong light confinement.[8,9] Their geometry provides a natural Fabry-Pérot optical cavity due to a characteristic elongated shape and relatively high modal refractive index ($n = 3 - 4$).[10,11] Nanowire lasers (NWLs) have been demonstrated across a wide range of operating wavelengths from ultraviolet[12–16] through visible[17,18] and to near infrared[19–22] by choosing a particular ternary alloy and stoichiometry composition. The quality of an optically-pumped NWL architecture is in part defined in terms of lasing threshold, the minimum power density required to produce lasing emission.

Common approaches to optimize the lasing threshold of a NWL include the introduction of single or multiple quantum wells,[22–27] quantum dots[28,29] or photonic crystals.[16,30] These methods rely on optimizing either the luminescence quantum efficiency $QE = k_r/(k_r + k_{nr})$ (where k_r and k_{nr} are the radiative and non-radiative rates, respectively[31]) or the mode-gain spatial overlap.[25] In some III-V semiconductor nanowires (notably GaAs), a significant challenge arises from the large surface-to-volume ratio leading to a high density of surface states[32] and large non-radiative recombination rate. To compensate for surface recombination effects it is possible to passivate the nanowire surface and reduce k_{nr}, for instance by plasma passivation,[33] surface nitridation,[34] metallic oxide deposition[35] or adding a thin cap layer of a higher band gap alloy.[36,37] Alternatively, QE may be improved by increasing k_r; one method to achieve this is through heavily doping the nanowire active region.[38–40] We have recently shown that room-temperature lasing in GaAs nanowires can be achieved by heavy p-type doping with Zn.[41] However, identifying an exact relationship between doping level and laser threshold is complicated by other mechanisms that contribute to lasing threshold; geometric effects such as cavity length (and distributed losses) , cavity diameter (and confinement), and large end-facet reflectivity variations from wire-to-wire, both of which may depend themselves on doping level and growth conditions. Recently, it has been reported that heavy doping has an impact on nanowire growth in particular for GaAs[42] and InP,[43] and can be beneficial in photodetector applications.[44] To elucidate the relationship between doping level and other nanowire characteristics, a fast and reliable technique to measure doping in single nanowires is of particular interest. In recent years, a number of optical approaches based on modeling photoluminescence (PL) spectra have been developed and applied to different nanowire architectures, including p-doped InP,[45] n-doped $In_xGa_{(1-x)}P$[46] and p-doped GaAs.[47] Here, we adopt a fast and simple phenomenological model based on shifts in PL spectra which allow us to rapidly and confidently determine local doping levels.

In this work we present a large-scale optoelectronic characterization of 975 p-doped GaAs nanowires using a previously reported statistical methodology,[48] and describe a facile optical

method of determining p-doping from PL spectra fitting. By investigating the correlation between PL intensity, p-doping level, nanowire length L, electronic disorder σ and lasing peak wavelength λ_{pk} with lasing threshold, we identify doping level and cavity length as the most important factors determining lasing threshold. Using low-power (below lasing threshold) excitation we report a non-monotonic increase in integrated PL intensity as a function of zinc concentration which can be modeled using a rate equation approach to extract the non-radiative recombination rate k_{nr} $=(0.14 \pm 0.04)\,\mathrm{ps}^{-1}$. For our highest doped growth, the number of NWLs showing room temperature lasing was 655 (67%) with a median threshold excitation energy of $60^{+38}_{-29}\,\mu\mathrm{J\ cm}^{-2}$ (where the upper and lower limits indicate the inter-quartile range). The nanolaser with best performance was identified from this set, with a threshold energy of $\sim$10 $\mu\mathrm{J\ cm}^{-2}$. Furthermore, by pre-selecting nanowires with high doping levels and long lengths through a simple spectroscopic and imaging approach we show that we can easily identify sub-populations with lasing yields of over 90%. Taken together, we show that a statistical approach is a powerful method for characterizing, understanding, and directing optimization for NWLs.

Four sets of GaAs nanowires were grown on (111)B GaAs substrates with different vapor-phase zinc dopant precursor levels (DEZn) using metal-organic vapour phase epitaxy (MOVPE). These nanowires were grown via a Au-catalyzed vapour-liquid-solid mechanism, similar to those previously reported,[41] and are labelled NW-A, NW-B, NW-C and NW-D corresponding to DEZn flow rates 47, 7.9, 3.6 and 0.6 μmol/min respectively. Each sample was prepared by dispersing the wires in iso-propylalcohol by ultrasonication, and deposition onto z-cut quartz substrates; multiple drops were used to control the nanowire density and uniformity. Initially $\sim$1000 nanowires were located and investigated from each sample using optical imaging machine vision and micro-photoluminescence (μ-PL) spectroscopy. From optical microscopy imaging (images shown in Figure S1 in the **Supporting Information**) we found a non-monotonic relationship between average nanowire length and DEZn flow rate, with an initial increase in length with DEZn flow followed by a reduction for the highest

doping levels to $l = 3.5 \pm 0.5\,\mu$m for NW-A (results shown in Figure S2 in the **Supporting Information**). While growth mechanism modelling[49] lies beyond the scope of this report, this suggests that nanowire growth is inhibited at higher Zn flow, as previously observed for InP nanowires,[50,51] with implications for growth strategies requiring highly doped and long nanowires. PL measurements under low-power excitation showed nanowires from sample set NW-A had the highest integrated emission intensity; this sample set was therefore selected for the following in-depth optical and statistical studies. The nanowire diameter for NW-A was measured using SEM (Figure S4 in the **Supporting Information**), revealing slight tapering and a typical diameter of $370 \pm 60\,$nm. We note that variations in nanowire diameter are expected to impact the dominant transverse mode,[52] which in turn can have a non-linear influence on lasing threshold.

PL measurements were carried out on 11227 nanowires from sample NW-A, from which 975 nanowires were randomly selected for more detailed characterization; this sample size reduction was required to limit the experimental time. The detailed studies included both lasing behavior using power-dependent μ-PL and spatial variations in doping using PL mapping. A number of optical approaches have been used to calculate p-doping (or Zn level) within GaAs; these typically relate shifts in the apparent band-edge emission to doping level.[53–56] To determine doping we used the effective band-gap energy E_g extracted for all 975 nanowires. According to Borghs et al., the band gap of GaAs has been observed to shrink as a consequence of heavy p-type doping, by $\Delta E_g = E_{GaAs} - E_g$,[53] where E_{GaAs} is the energy band gap of intrinsic GaAs. The hole concentration can be modeled by the empirically determined equation

$$p^+ = \left(\frac{\Delta E_g}{K}\right)^3 . \tag{1}$$

where K is a constant. While literature values for K exist, we independently determined a value for K=(1.15±0.03)×10^{-8} eV·cm in our microscopy system using three planar reference samples with carrier concentration measured by SIMS, and additional Zn density confirma-

tion by using XPS and Raman techniques (data and discussion of these measurements is provided in the **Supporting Information**).

We calculate the effective band gap energy E_g by fitting the intensity $I(E)$ of measured PL with a convolution between a 3D density of states $D(E)$ and a Gaussian $G(E)$ distribution function multiplied by a scaling factor α as reported in previous studies.[48,57] Briefly,

$$I(E) = \alpha(D(E) \otimes G(E)), \tag{2}$$

where $D(E)$ is given by

$$D(E) \propto \sqrt{E - E_g} \exp\left(-\frac{E - E_g}{k_B T}\right). \tag{3}$$

Here E is the photon energy and T is the electron temperature, which was fixed at 300K. $G(E)$ is given by

$$G(E) = \exp\left(\frac{-E^2}{2\sigma^2}\right), \tag{4}$$

where σ is a phenomenological parameter describing the electronic disorder present in the emission, which we use to parameterize spectral broadening from all sources including that caused by inhomogeneity from crystal defects[48,57] or p-doping variation across the excitation spot. We note that the p-doping level of nanowires has previously been determined using the emission full-width-at-half-maximum (FWHM); however, Lindgren and colleagues explained that this approach is inaccurate at room temperature for higher doping concentrations.[45] We observe that electronic disorder (related to the FWHM) appears constant for most of the p-doping values range (see **Supporting Information**), therefore, we took the approach described in Equation 1 as the preferred method for determining the value for the doping level. Figure 1 shows a PL spectrum from a typical nanowire under weak excitation. A fit using Equation 2 is able to reproduce the PL nanowire emission accurately; a discrepancy at the low energy tail (1.3 eV) is attributed to residual strain or material imperfections.[57–59]

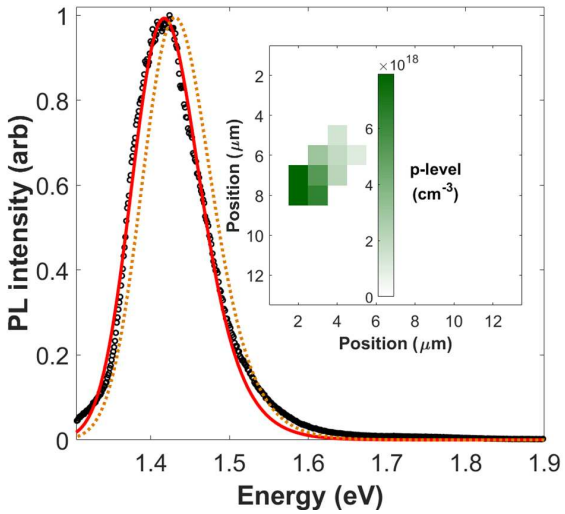

Figure 1: PL spectrum of a typical nanowire (black circles) and a fit as described in the text (red line). The predicted PL from undoped GaAs is given by the orange dotted curve, demonstrating the PL shift due to doping. The inset shows a p-doping map for this wire, doping level corresponding to each point was calculated using Equation 1.

It is known that axial variation in growth can exist both in the present nanowires (which are produced using a two-step "nucleation and growth" approach[60]) and in general.[59] To obtain a meaningful measure of p-doping, a confocal PL emission map for each nanowire was made with a $\sim$0.5 μm spatial resolution, and the emission for each point fitted with the model described by Equation 1. Using this, a doping map was created (as shown in the inset of Figure 1), allowing the maximum, minimum and mean doping level to be determined for every wire.

Figure 2a shows a histogram of mean p-doping level measured in sample NW-A. A significant distribution in doping concentration values is observed for the 975 nanowires set, with a median value of $3.6^{+1.3}_{-1.1}\times10^{18}$ cm^{-3}, where the upper and lower limits represent the interquartile range. This distribution in doping provides an inherent parameter space to allow us to investigate the relationship between doping level and optoelectronic performance. Figure 2b shows IQE (under weak excitation conditions) as a function of mean p-doping level, where nanowire emission tends to become brighter with increasing p-doping as previously observed.[53] While length, orientation, and defect density might be expected to influence the

integrated PL from each wire, a strength in our statistical approach is the ability to isolate the effect of each parameter. As such, a simple model for emission intensity can be written by approximating the PL intensity as proportional to internal quantum efficiency IQE such that

$$I(p) = \beta \mathrm{IQE}(p) = \beta \left(\frac{B(p)p}{B(p)p + C(p)p^2 + k_{nr}} \right) \tag{5}$$

where $B(p)$ is the doping dependent radiative recombination rate, as reported by Nelson and Sobers,[31] and given by

$$B(p) = -3.47 \times 10^{-11} \ln(p) \ \mathrm{cm^3 s^{-1}} + 1.63 \times 10^{-9} \ \mathrm{cm^3 s^{-1}}, \tag{6}$$

and $C(p)$ is the doping dependent Auger rate, as found by Ahrenkiel et al.,[61] given by

$$C(p) = 3.83 \times 10^{-43} p^{0.78} \ \mathrm{cm^6 s^{-1}}. \tag{7}$$

The two fitting parameters, β and k_{nr}, are an arbitrary scaling factor and the non-radiative rate respectively. While β may depend on a variety of geometrical and experimental factors for each NW, by averaging over our large population we are able to identify any trend in emission intensity with p-doping.

By fitting the data in Figure 2b with the model in Equation 5, a value for k_{nr} of $(0.14 \pm 0.04)\,\mathrm{ps^{-1}}$ was determined. In unpassivated nanowires, we anticipate that the majority of recombination will occur at the surface;[62] by approximating $k_{nr} \geq 4S/d$, where S is the surface recombination velocity (SRV) and d is the NW diameter measured as $370 \pm 60\,\mathrm{nm}$ (Figure S4), we can extract a value of $S = (13 \pm 4) \times 10^5\,\mathrm{cm/s}$. This is in agreement with values measured using both time-resolved photoluminescence spectroscopy[41] on the same wires ($20 \times 10^5\,\mathrm{cm/s}$) and those measured using terahertz spectroscopy[32] on undoped GaAs nanowires ($5.4 \times 10^5\,\mathrm{cm/s}$). This agreement is notable considering our simple approach

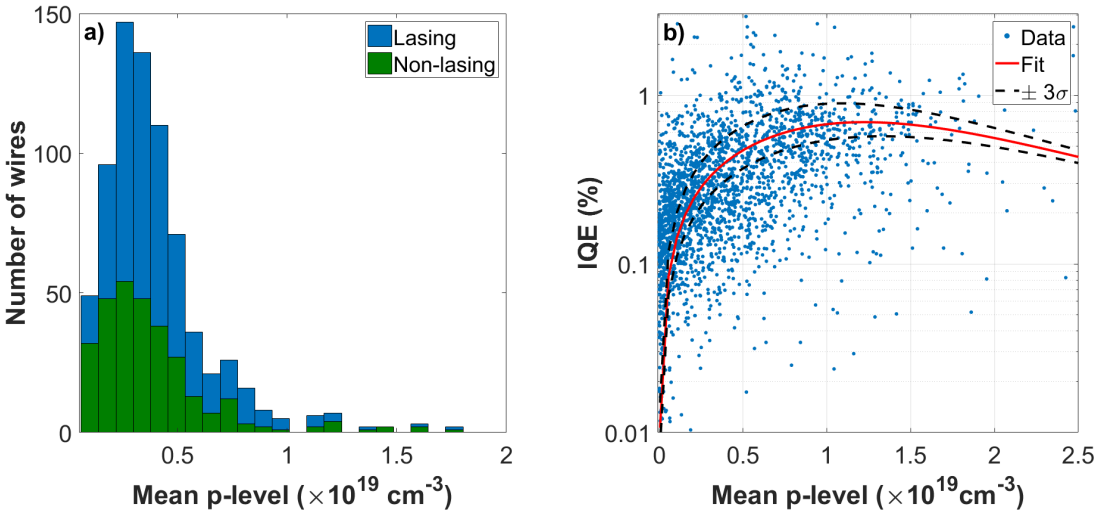

Figure 2: a) Stacked histogram showing mean p-doping distribution for a total of 975 nanowires from sample NW-A. The occurrence of doping levels within lasing (blue) and non-lasing (green) sub-groups is indicated. b) Internal quantum efficiency as a function of mean p-doping concentration shown in blue. The red curve and black dashed lines show the fit according to Equation 5 and 3σ confidence bounds, respectively.

studies a single growth with a low-cost and low-excitation power technique; we however note that by neglecting bulk recombination, our value for S represents a maximum surface recombination velocity for these nanowires.

One notable feature of the fit shown in Figure 2b is the emergence of a plateau in IQE at doping levels of around $1.2 \times 10^{19}\,\mathrm{cm}^{-3}$. Above this value, non-radiative recombination via the Auger mechanism begins to dominate over radiative bimolecular recombination, reducing IQE. As such, the NW-A batch represent the maximum possible IQE for Zn-doped GaAs nanowires with this architecture; to achieve higher IQE, non-radiative recombination must be addressed through surface passivation or optimized growth conditions. Considering a surface-passivated GaAs nanowire[63,64] with a non-radiative rate k_{nr} $\approx 1\,\mathrm{ns}^{-1}$ and a doping level of $2\times10^{18}\,\mathrm{cm}^{-3}$ we may predict an improvement in IQE, with values of up to 20% being achievable.

Lasing behavior was studied for each wire under sub-picosecond optical excitation at 620 nm (details in **Supporting Information**), and the PL as a function of pulse power

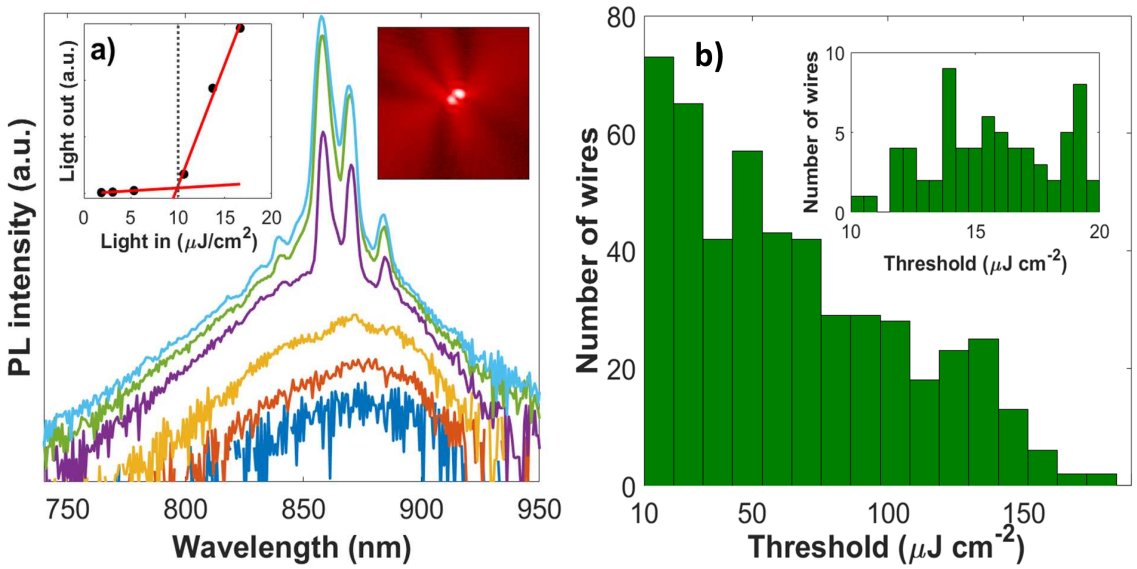

Figure 3: a) Plot showing PL spectra from the best-in-class nanowire. The lasing threshold energy is calculated from the light in vs light out as $\sim$10 μJ cm^{-2} (as shown in the left inset by a dotted line). The inset in the upper right shows the diffraction pattern for this wire characteristic of lasing emission in resonant cavities. The image is taken from optical microscopy at the emission wavelength above threshold. b) Histogram of lasing threshold values for a total of 453 nanolasers. The inset shows a higher resolution view of the low threshold region between 10-20 μJ cm^{-2} .

was measured for the 975 nanowires at room temperature. For each nanowire a light in vs integrated light out (LILO) curve was made to allow for algorithmic determination of lasing. A set of fluence-dependant spectra is shown in Figure 3a, along with the associated LILO curve. The conditions for lasing were defined as an abrupt change in gradient of the LILO curve along with the appearance of a narrow emission peak with a FWHM $<$5 nm and a peak height of $>$30% of the overall PL. A linear fit was made to the spontaneous and stimulated emission regimes on the LILO curve, and the lasing threshold energy was taken as the intersection of the two lines; while this over-estimates the true threshold, this approach was seen to be more robust when only limited number of data-points are measured for each nanowire. All nanowires displaying optically verified lasing behavior were included in calculations of the total lasing yield, the fraction of NWL showing lasing at room temperature from sample NW-A was 655 wires (67%). The remaining wires either did not show any signs of lasing at maximum excitation fluence (250 μJ cm^{-2}), or the PL intensity was observed to

drop due to the onset of thermal degradation. For an in-depth correlation study, $\sim$ 30% of wires had to be cut from the 655 nanowire set due to low confidence in PL fitting or lasing threshold energy estimation; this narrowed the number of nanowires used for correlation studies to 453 .

Given the importance of IQE to emission as shown in Figure 2b, the doping level might be expected to be the most important parameter determining yield. The distribution in mean doping concentration for subsets of the 975 nanowires which either lased or were non-lasing is presented in Figure 2a. While it appears that lasing nanowires are much more likely to occur for higher concentration, it is also clear that many nanowires from the non-lasing group have doping levels which overlap with the lasing subset; this is a strong indication that other geometrical or material parameters such as non-planar end facets, crystal defects and/or nanowire length play a significant role in determining the likelihood of room-temperature lasing in this architecture.

Figure 3b shows the distribution of lasing threshold values for nanowires from sample NW-A, ranging from $\sim$10 to $\sim$150 μJ cm^{-2} with a median value of 60^{+38}_{-29} μJ cm^{-2} , where the upper and lower limits represent the interquartile range. This range of lasing threshold values are amongst the lowest reported in the literature for a room temperature NWL; in particular, the best-in-batch nanowire has a lasing threshold of 10 μJ cm^{-2} with a mean Zn doping level of $(0.8\pm0.1)\times10^{19}$ cm^{-3}. Figure 3a shows room-temperature PL spectra of the best-in-batch nanowire at increasing excitation intensity. At low pump fluence (2-6 μJ cm^{-2}) a broad PL emission associated with the spontaneous emission is observed. Above 10 μJ cm^{-2} three narrow peaks, associated with Fabry-Pérot cavity modes, appear at 858 nm, 870 nm and 884 nm. With increasing fluence the integrated PL intensity increases with a higher gradient onset in the lasing regime, as shown in the inset. Coherent emission from this nanowire was confirmed by optical imaging at the emission wavelength as shown in the top right inset of Figure 3a; the image shows the characteristic diffraction pattern associated with a short-cavity Fabry-Pérot laser.[52]

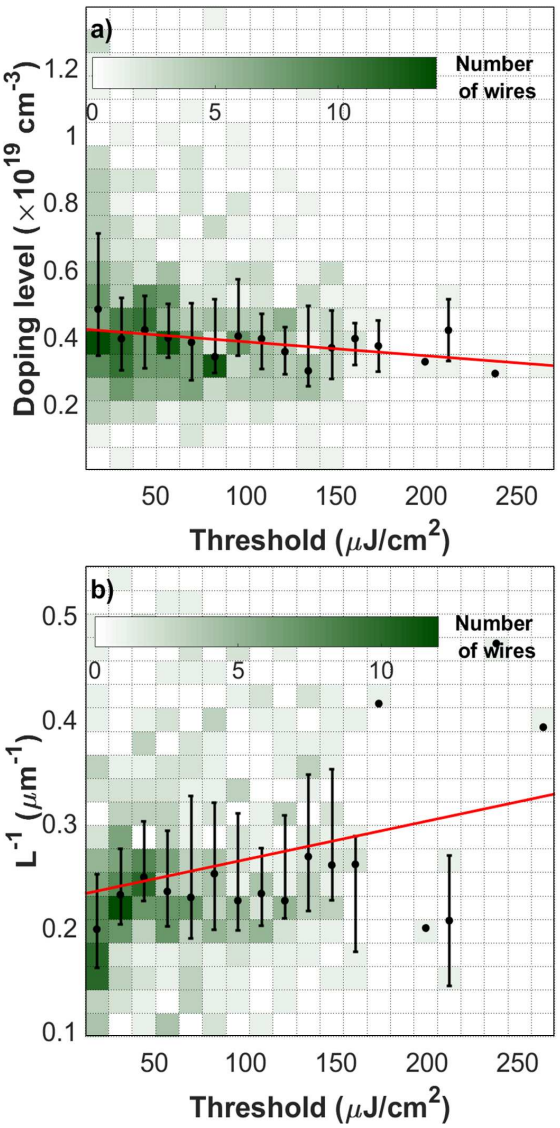

Figure 4: 2D histogram showing lasing threshold and a) mean doping level and b) nanowire inverse length. Points and error bars indicate the median and interquartile range within each threshold bin, and a linear guide to the eye is given in red. A moderate but statistically significant correlation is observed for both variables (linear correlation coefficient of a) $\rho = -0.19$ and b) $\rho = 0.15$).

To investigate the relative influence of doping on distributed losses, the mean doping level determined for 453 nanowires were compared with lasing threshold. The 2D histogram shown in Figure 4a shows a moderate negative linear correlation between Zn concentration and lasing threshold (linear correlation coefficient $\rho = -0.19$, significance $p \ll 0.05$). This result is in accordance with the correlation observed in the low-power PL study (Figure 2b), supporting the role of quantum efficiency in determining lasing threshold.

While doping level is important for high quantum efficiency, cavity geometry is also critical for lasing. The threshold gain g_{th} required for lasing in a monolithic cavity can be approximated as

$$g_{th} = \alpha_0 - \frac{\ln(R_1 R_2)}{2L},$$

where α_0 represents the distributed losses, $R_{1,2}$ are the reflectivity coefficients of the two end mirrors and L is the cavity length. The Au nanoparticle present in these wires is expected to improve the reflectivity at one of the end-facets as reported by Saxena et al.[52] which may contribute to lower threshold gain. Each nanowire length was calculated from the peak separation of the Fabry-Pérot modes from the lasing data (see **Supporting Information**); to minimize measuring multiple transverse cavity modes which can be supported in this architecture which might interfere with the length calculation, we used the lasing spectra just above threshold. To study the relative importance of distributed and end-mirror losses, the correlation between nanowire inverse length and lasing threshold was measured and is shown in Figure 4b (linear correlation coefficient ρ=0.15, significance p=0.01). This positive correlation, while moderate, suggests that wires with a longer length will compensate for mirror losses and have lower threshold values. A number of other correlations which were also investigated include a significant inverse correlation between lasing peak wavelength and lasing threshold (see **Supporting Information**), attributed to a gain spectral blueshift under higher excitation conditions required for wires with a high threshold gain.

In commercial or industrial applications, lasing yield fraction is a vital figure of merit for any NWL architecture. We studied the lasing yield in terms of the two critical parameters:

p-doping level from low-power PL and nanowire length as determined simply from optical microscopy. These techniques allow the rapid measurement of doping and length, which can be performed in less than 1 second per nanowire. By selecting nanowires based on their measured doping and length, the yield (defined as the ratio between the number which showed lasing to the total wires considered) was calculated for different subsets of wires. Figure 5a,b shows the yield as function of subset; the yield for nanowires with doping $p > p_{\mathrm{cut}}$ and length $L > L_{\mathrm{cut}}$ is shown as a function of p_{cut} or L_{cut}, respectively. It was found that wires with a mean doping level $> 3{\times}10^{18}\,\mathrm{cm}^{-3}$ had the highest chance of lasing with a yield of $\sim 65\%$ (Figure 5a). From a study as a function of length, we found that the likelihood of lasing increases to $\sim$70 % for nanowires with a length $>4\,\mu$m (Figure 5b). By combining these two requirements it is possible to define sub-populations within the growth ensemble with significantly increased yields; by selecting nanowires with $p > p_{\mathrm{cut}} = 0.3{\times}10^{19}\,\mathrm{cm}^{-3}$ and $L > L_{\mathrm{cut}} = 4\,\mu$m we cut out 75% of the total nanowires within the growth batch, but we hope to achieve a lasing yield of at least $\sim 70\%$. Figure 5c shows the yield as a 2D histogram as a function of length and p-doping.

To validate this approach, a new and previously unstudied sample was prepared from the same NW-A nanowire growth. By performing rapid doping and length calculations from 553 single nanowire PL and optical images, a sub-population of 131 nanowires was selected according to the cut values determined above. From this 131 NW subset, 120 (93 %) showed lasing with a median lasing threshold of $55^{+20}_{-11}\,\mu\mathrm{J\ cm}^{-2}$ (see **Supporting Information** for data and details). As expected, the median threshold is close to (and slightly lower than) that determined from the initial sample ($60^{+38}_{-29}\,\mu\mathrm{J\ cm}^{-2}$). This approach demonstrates that it is not only possible to use the correlative methodology to understand the relative importance of controllable parameters on functional performance, but also to specify a subset with higher yield and potentially lower lasing threshold.

In summary, we have demonstrated a method to simply assess nanowire p-doping using a large-scale optical methodology. To measure a meaningful carrier concentration in each

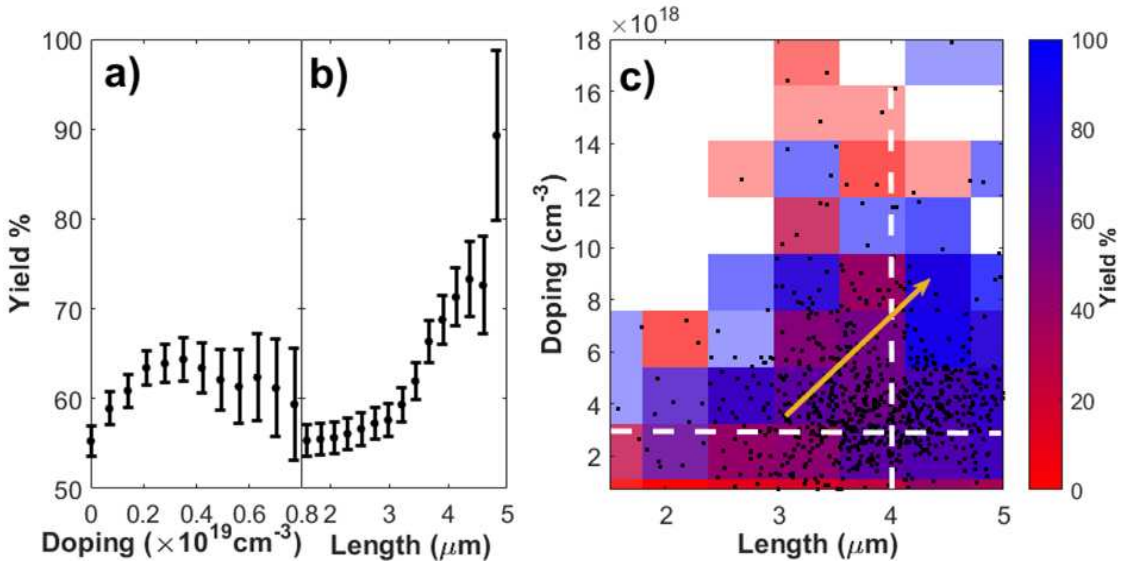

Figure 5: Yield of nanowires lasers for a series of selection cuts; for sub-populations a) where the doping level p exceeds some value p_{cut} and b) where the length L exceeds some value L_{cut}. c) 2D histogram of lasing yield associated to length and p- doping distributions. Yields of over 70% are predicted where sub-populations are selected on both yield and length. Black dots indicate individual nanowires, and the yellow arrow indicates the region of highest yield. White dashed lines indicate the selected cut values p_{cut} and L_{cut}.

nanowire, we found that it was essential to determine the mean doping level from individual nanowire PL mapping. The calculated p-doping values were within the expected nominal range as confirmed by planar reference samples (see **Supporting Information**). Photoluminescence intensity is enhanced for higher doping levels as predicted by a model relating IQE to doping, with an increase in functional performance further confirmed by lower lasing threshold energy and high lasing yield for wires with an increased doping level. We have demonstrated that the primary controllable factors for determining lasing threshold in p-doped nanowires are doping level and nanowire length. As limited opportunity exists for increasing performance through increased doping due to Auger recombination, reducing k_{nr} should be the preferred strategy for improving NWLs. A best-in-class nanowire laser threshold of $10\,\mu\text{J cm}^{-2}$ was measured, indicating that this architecture is of technological relevance. Finally, by using facile spectroscopic and imaging measurements we demonstrate arbitrarily high-yield subsets can be identified from a sufficiently large ensemble, and we

show a subset with a lasing yield of 93%.

Semiconductor nanolasers based on heavily p-doped materials are a strong candidate architecture for low-threshold performance, paving the route towards electrically pumped operation in industrial applications. Moreover, our presented methodology may be applied to a wide range of optoelectronic nanomaterials to study key parameters for improved functional performance as well as assessing growth homogeneity.

Author Contributions

The project was led by JAA and PP, with data taken and analyzed by JAA. XT contributed additional analysis. The nanolasers were designed by TB, DS and SM, and grown by ML under the supervision of HHT and CJ. XPS analysis was performed by SS and ASW. Raman measurements were carried out by JAA and PM. The manuscript was primarily written by JAA and PP, with contributions from all authors.

Acknowledgement

We thank the Australian National Fabrication Facility (ANFF) ACT node for access to the epitaxy, fabrication and characterization facilities used in this work, and Dr. Li Li for assisting with SEM. PP acknowledges the support of the Royal Society (RG140411). JAA acknowledges a CONACyT-SENER funded scholarship. PM acknowledges financial support from the EPSRC (EP/R01146X/1). TB, DS, SM, ML, HHT and CJ acknowledge financial support from the Australian Research Council.

Supporting Information Available

Experimental details for low-power and power-dependent photoluminescence. Nanowire lengths from optical imaging and machine vision. Fabry-Pérot length calculations. SEM

imagery and nanowire geometry. Analysis of planar doped samples by photoluminescence, XPS and Hall effect measurements. Additional correlations between parameters. Additional power dependence study based on yield-cuts. This material is available free of charge via the Internet at `http://pubs.acs.org/`.

References

(1) Law, M. *Science* **2004**, *305*, 1269–1273.

(2) Ma, R. M.; Yin, X.; Oulton, R. F.; Sorger, V. J.; Zhang, X. *Nano Letters* **2012**, *12*, 5396–5402.

(3) Shen, Y.; Harris, N. C.; Skirlo, S.; Prabhu, M.; Baehr-Jones, T.; Hochberg, M.; Sun, X.; Zhao, S.; Larochelle, H.; Englund, D.; Soljačić, M. *Nature Photonics* **2017**, *11*, 441–446.

(4) Alexander-Webber, J. A.; Groschner, C. K.; Sagade, A. A.; Tainter, G.; Gonzalez-Zalba, M. F.; Di Pietro, R.; Wong-Leung, J.; Tan, H. H.; Jagadish, C.; Hofmann, S.; Joyce, H. J. *ACS Applied Materials & Interfaces* **2017**, *9*, 43994–44000.

(5) Baig, S. A.; Boland, J. L.; Damry, D. A.; Tan, H. H.; Jagadish, C.; Joyce, H. J.; Johnston, M. B. *Nano Letters* **2017**, *17*, 2603–2610.

(6) Greytak, A. B.; Barrelet, C. J.; Li, Y.; Lieber, C. M. *Applied Physics Letters* **2005**, *87*, 1–3.

(7) Röder, R.; Ronning, C. *Semiconductor Science and Technology* **2018**, *33*, 033001.

(8) Pauzauskie, P. J.; Yang, P. *Materials Today* **2006**, *9*, 36–45.

(9) Haffouz, S.; Zeuner, K. D.; Dalacu, D.; Poole, P. J.; Lapointe, J.; Poitras, D.; Mnaymneh, K.; Wu, X.; Couillard, M.; Korkusinski, M.; Schöll, E.; Jöns, K. D.; Zwiller, V.; Williams, R. L. *Nano Letters* **2018**, *18*, 3047–3052.

(10) Parkinson, P.; Alanis, J. A.; Peng, K.; Saxena, D.; Mokkapati, S.; Jiang, N.; Fu, L.; Tan, H. H.; Jagadish, C. *Nano Futures* **2018**, *2*, 035004.

(11) Couteau, C.; Larrue, A.; Wilhelm, C.; Soci, C. *Nanophotonics* **2015**, *4*, 90–107.

(12) Huang, M. H. *Science* **2001**, *292*, 1897–1899.

(13) Johnson, J. C.; Choi, H.-J.; Knutsen, K. P.; Schaller, R. D.; Yang, P.; Saykally, R. J. *Nature materials* **2002**, *1*, 106–110.

(14) Ding, J. X.; Zapien, J. A.; Chen, W. W.; Lifshitz, Y.; Lee, S. T.; Meng, X. M. *Applied Physics Letters* **2004**, *85*, 2361–2363.

(15) Chu, S.; Wang, G.; Zhou, W.; Lin, Y.; Chernyak, L.; Zhao, J.; Kong, J.; Li, L.; Ren, J.; Liu, J. *Nature Nanotechnology* **2011**, *6*, 506–510.

(16) Sergent, S.; Takiguchi, M.; Tsuchizawa, T.; Taniyama, H.; Kuramochi, E.; Notomi, M. *ACS Photonics* **2017**, *4*, 1040–1047.

(17) Agarwal, R.; Barrelet, C. J.; Lieber, C. M. *Nano Letters* **2005**, *5*, 917–920.

(18) Li, J.; Meng, C.; Liu, Y.; Wu, X.; Lu, Y.; Ye, Y.; Dai, L.; Tong, L.; Liu, X.; Yang, Q. *Advanced Materials* **2013**, *25*, 833–837.

(19) Chin, A. H.; Vaddiraju, S.; Maslov, A. V.; Ning, C. Z.; Sunkara, M. K.; Meyyappan, M. *Applied Physics Letters* **2006**, *88*, 1–4.

(20) Mayer, B.; Rudolph, D.; Schnell, J.; Morkötter, S.; Winnerl, J.; Treu, J.; Müller, K.; Bracher, G.; Abstreiter, G.; Koblmüller, G.; Finley, J. J. *Nature Communications* **2013**, *4*, 2931.

(21) Li, K.; Sun, H.; Ren, F.; Ng, K. W.; Tran, T. T. D.; Chen, R.; Chang-Hasnain, C. J. *Nano Letters* **2014**, *14*, 183–190.

(22) Stettner, T.; Thurn, A.; Döblinger, M.; Hill, M. O.; Bissinger, J.; Schmiedeke, P.; Matich, S.; Kostenbader, T.; Ruhstorfer, D.; Riedl, H.; Kaniber, M.; Lauhon, L. J.; Finley, J. J.; Koblmüller, G. *Nano Letters* **2018**, acs.nanolett.8b02503.

(23) Yan, X.; Wei, W.; Tang, F.; Wang, X.; Li, L.; Zhang, X.; Ren, X. *Applied Physics Letters* **2017**, *110*, 061104.

(24) Qian, F.; Li, Y.; Gradečak, S.; Park, H.-G.; Dong, Y.; Ding, Y.; Wang, Z. L.; Lieber, C. M. *Nature Materials* **2008**, *7*, 701–706.

(25) Saxena, D.; Jiang, N.; Yuan, X.; Mokkapati, S.; Guo, Y.; Tan, H. H.; Jagadish, C. *Nano Letters* **2016**, *16*, 5080–5086.

(26) Stettner, T.; Zimmermann, P.; Loitsch, B.; Döblinger, M.; Regler, A.; Mayer, B.; Winnerl, J.; Matich, S.; Riedl, H.; Kaniber, M.; Abstreiter, G.; Koblmüller, G.; Finley, J. J. *Applied Physics Letters* **2016**, *108*, 0–5.

(27) Lu, F.; Bhattacharya, I.; Sun, H.; Tran, T.-T. D.; Ng, K. W.; Malheiros-Silveira, G. N.; Chang-Hasnain, C. *Optica* **2017**, *4*, 717.

(28) Tatebayashi, J.; Kako, S.; Ho, J.; Ota, Y.; Iwamoto, S.; Arakawa, Y. *Nature Photonics* **2015**, *9*, 501–505.

(29) Wu, J.; Ramsay, A.; Sanchez, A.; Zhang, Y.; Kim, D.; Brossard, F.; Hu, X.; Benamara, M.; Ware, M. E.; Mazur, Y. I.; Salamo, G. J.; Aagesen, M.; Wang, Z.; Liu, H. *Nano Letters* **2016**, *16*, 504–511.

(30) Yokoo, A.; Takiguchi, M.; Birowosuto, M. D.; Tateno, K.; Zhang, G.; Kuramochi, E.; Shinya, A.; Taniyama, H.; Notomi, M. *ACS Photonics* **2017**, *4*, 355–362.

(31) Nelson, R. J.; Sobers, R. G. *Journal of Applied Physics* **1978**, *49*, 6103–6108.

(32) Joyce, H. J.; Docherty, C. J.; Gao, Q.; Tan, H. H.; Jagadish, C.; Lloyd-Hughes, J.; Herz, L. M.; Johnston, M. B. *Nanotechnology* **2013**, *24*, 214006.

(33) Herman, J. S.; Terry, F. L. *Applied Physics Letters* **1992**, *60*, 716–717.

(34) Alekseev, P. a.; Dunaevskiy, M. S.; Ulin, V. P.; Lvova, T. V.; Filatov, D. O.; Nezhdanov, A. V.; Mashin, A. I.; Berkovits, V. L. *Nano Letters* **2015**, *15*, 63–68.

(35) Huang, M. L.; Chang, Y. C.; Chang, C. H.; Lee, Y. J.; Chang, P.; Kwo, J.; Wu, T. B.; Hong, M. *Applied Physics Letters* **2005**, *87*, 1–3.

(36) Joyce, H. J.; Parkinson, P.; Jiang, N.; Docherty, C. J.; Gao, Q.; Tan, H. H.; Jagadish, C.; Herz, L. M.; Johnston, M. B. *Nano Letters* **2014**, *14*, 5989–5994.

(37) Haggren, T.; Jiang, H.; Kakko, J. P.; Huhtio, T.; Dhaka, V.; Kauppinen, E.; Lipsanen, H. *Applied Physics Letters* **2014**, *105*.

(38) Haggren, T.; Kakko, J. P.; Jiang, H.; Dhaka, V.; Huhtio, T.; Lipsanen, H. Effects of Zn doping on GaAs nanowires. 14th IEEE International Conference on Nanotechnology, IEEE-NANO 2014. 2014; pp 825–829.

(39) Boland, J. L.; Conesa-Boj, S.; Parkinson, P.; Tütüncüoglu, G.; Matteini, F.; Rüffer, D.; Casadei, A.; Amaduzzi, F.; Jabeen, F.; Davies, C. L.; Joyce, H. J.; Herz, L. M.; Fontcuberta I Morral, A.; Johnston, M. B. *Nano Letters* **2015**, *15*, 1336–1342.

(40) Troian, A.; Otnes, G.; Zeng, X.; Chayanun, L.; Dagytė, V.; Hammarberg, S.; Salomon, D.; Timm, R.; Mikkelsen, A.; Borgström, M. T.; Wallentin, J. *Nano Letters* **2018**, acs.nanolett.8b02957.

(41) Burgess, T.; Saxena, D.; Mokkapati, S.; Li, Z.; Hall, C. R.; Davis, J. A.; Wang, Y.; Smith, L. M.; Fu, L.; Caroff, P.; Tan, H. H.; Jagadish, C. *Nature Communications* **2016**, *7*, 11927.

(42) Czaban, J. A.; Thompson, D. A.; LaPierre, R. R. *Nano Letters* **2009**, *9*, 148–154.

(43) Yee, R. J.; Gibson, S. J.; Dubrovskii, V. G.; LaPierre, R. R. *Applied Physics Letters* **2012**, *101*, 263106.

(44) Ali, H. et al. *Small* **2018**, *14*, 1704429.

(45) Lindgren, D.; Hultin, O.; Heurlin, M.; Storm, K.; Borgström, M. T.; Samuelson, L.; Gustafsson, A. *Nanotechnology* **2015**, *26*, 045705.

(46) Xulu, Z. *Nanotechnology* **2018**, 1361–6528.

(47) Isik, N.; Fiordaliso, E. M.; LaPierre, R. R. *Nanotechnology* **2018**, *29*, 234001.

(48) Alanis, J. A.; Saxena, D.; Mokkapati, S.; Jiang, N.; Peng, K.; Tang, X.; Fu, L.; Tan, H. H.; Jagadish, C.; Parkinson, P. *Nano Letters* **2017**, *17*, 4860–4865.

(49) Dubrovskii, V. G.; Sibirev, N. V.; Berdnikov, Y.; Gomes, U. P.; Ercolani, D.; Zannier, V.; Sorba, L. *Nanotechnology* **2016**, *27*, 375602.

(50) Borgstrom, M. T.; Norberg, E.; Wickert, P.; Nilsson, H. A.; Tragardh, J.; Dick, K. A.; Statkute, G.; Ramvall, P.; Deppert, K.; Samuelson, L. *Nanotechnology* **2008**, *19*, 445602.

(51) Wallentin, J.; Ek, M.; Wallenberg, L. R.; Samuelson, L.; Deppert, K.; Borgstrom, M. T. *Nano Letters* **2010**, *10*, 4807–4812.

(52) Saxena, D.; Mokkapati, S.; Parkinson, P.; Jiang, N.; Gao, Q.; Tan, H. H.; Jagadish, C. *Nature Photonics* **2013**, *7*, 963–968.

(53) Borghs, G.; Bhattacharyya, K.; Deneffe, K.; Van Mieghem, P.; Mertens, R. *Journal of Applied Physics* **1989**, *66*, 4381–4386.

(54) Jain, S. C.; Roulston, D. J. *Solid-State Electronics* **1991**, *34*, 453–465.

(55) Ky, N. H.; Pavesi, L.; Araújo, D.; Ganière, J. D.; Reinhart, F. K. *Journal of Applied Physics* **1991**, *69*, 7585–7593.

(56) Dagyte, V.; Barrigon, E.; Zhang, W.; Zeng, X.; Heurlin, M.; Otnes, G.; Anttu, N.; Borgström, M. T. *Nanotechnology* **2017**, *28*, 505706.

(57) Davies, C. L.; Parkinson, P.; Jiang, N.; Boland, J. L.; Conesa-Boj, S.; Tan, H. H.; Jagadish, C.; Herz, L. M.; Johnston, M. B. *Nanoscale* **2015**, *7*, 20531–20538.

(58) Chen, Y.; Cingolani, R.; Andreani, L. C.; Bassani, F.; Massies, J. *Il Nuovo Cimento D* **1988**, *10*, 847–859.

(59) Bolinsson, J.; Ek, M.; Trägårdh, J.; Mergenthaler, K.; Jacobsson, D.; Pistol, M. E.; Samuelson, L.; Gustafsson, A. *Nano Research* **2014**, *7*, 1–18.

(60) Joyce, H. J.; Gao, Q.; Tan, H. H.; Jagadish, C.; Kim, Y.; Zhang, X.; Guo, Y.; Zou, J. *Nano Letters* **2007**, *7*, 921–926.

(61) Ahrenkiel, R. K.; Ellingson, R.; Metzger, W.; Lubyshev, D. I.; Liu, W. K. *Applied Physics Letters* **2001**, *78*, 1879–1881.

(62) Parkinson, P.; Joyce, H. J.; Gao, Q.; Tan, H. H.; Zhang, X.; Zou, J.; Jagadish, C.; Herz, L. M.; Johnston, M. B. *Nano Letters* **2009**, *9*, 3349–3353.

(63) Jiang, N.; Parkinson, P.; Gao, Q.; Breuer, S.; Tan, H. H.; Wong-Leung, J.; Jagadish, C. *Applied Physics Letters* **2012**, *101*, 023111.

(64) Jiang, N.; Gao, Q.; Parkinson, P.; Wong-Leung, J.; Mokkapati, S.; Breuer, S.; Tan, H. H.; Zheng, C. L.; Etheridge, J.; Jagadish, C. *Nano Letters* **2013**, *13*, 5135–5140.

Graphical TOC Entry